

Long-Range Neuronal Circuits Underlying the Interaction between Sensory and Motor Cortex

Tianyi Mao,^{1,2} Deniz Kusefoglu,^{1,2} Bryan M. Hooks,¹ Daniel Huber,¹ Leopoldo Petreanu,¹ and Karel Svoboda^{1,*}

¹Janelia Farm Research Campus, HHMI, 19700 Helix Drive, Ashburn, VA 20147, USA

²Present address: Vollum Institute, Oregon Health & Science University, Portland, OR 97239, USA

*Correspondence: svobodak@janelia.hhmi.org

DOI 10.1016/j.neuron.2011.07.029

SUMMARY

In the rodent vibrissal system, active sensation and sensorimotor integration are mediated in part by connections between barrel cortex and vibrissal motor cortex. Little is known about how these structures interact at the level of neurons. We used Channelrhodopsin-2 (ChR2) expression, combined with anterograde and retrograde labeling, to map connections between barrel cortex and pyramidal neurons in mouse motor cortex. Barrel cortex axons preferentially targeted upper layer (L2/3, L5A) neurons in motor cortex; input to neurons projecting back to barrel cortex was particularly strong. Barrel cortex input to deeper layers (L5B, L6) of motor cortex, including neurons projecting to the brainstem, was weak, despite pronounced geometric overlap of dendrites with axons from barrel cortex. Neurons in different layers received barrel cortex input within stereotyped dendritic domains. The cortico-cortical neurons in superficial layers of motor cortex thus couple motor and sensory signals and might mediate sensorimotor integration and motor learning.

INTRODUCTION

Rodents move their large whiskers, also called facial vibrissae, through space to locate and identify objects (Carvell and Simons, 1990; Hutson and Masterton, 1986; Knutsen et al., 2006; Krupa et al., 2001; O'Connor et al., 2010a). Conversely, whisker movements are guided by sensory feedback (Mitchinson et al., 2007; Nguyen and Kleinfeld, 2005). These interactions between sensory and motor systems are crucial for haptic perception (Diamond et al., 2008; Gibson, 1962; Wolpert et al., 1995). Sensorimotor integration in whisker-based somatosensation is mediated by brain structures that form a series of nested loops, at the levels of the brainstem, thalamus, and cerebral cortex (Diamond et al., 2008; Kleinfeld et al., 1999). Little is known about the cellular architecture of these different loops.

A prominent loop occurs at the level of the cerebral cortex (Aronoff et al., 2010; Chakrabarti and Alloway, 2006; Donoghue and Parham, 1983; Ferezou et al., 2007; Hoffer et al., 2003; Izraeli and

Porter, 1995; Miyashita et al., 1994; Porter and White, 1983; Veinante and Deschênes, 2003; Vogt and Pandya, 1978; Welker et al., 1988; White and DeAmicis, 1977). Vibrissal primary sensory cortex (vS1, barrel cortex) and vibrissal primary motor cortex (vM1) are reciprocally connected. One barrel column in vS1 projects to a band of vM1, with its long axis in the anterior/posterior (A/P) direction (Aronoff et al., 2010). vM1 projects diffusely to vS1, covering most of the barrel field and adjacent areas (Veinante and Deschênes, 2003).

Reciprocal cortical connections have also been detected in neurophysiological recordings in vivo. Following the deflection of a whisker, excitation first ascends into vS1 and then rapidly propagates to vM1 (Farkas et al., 1999; Ferezou et al., 2007; Kleinfeld et al., 2002). Neuronal activity in vS1 is modulated by whisking (Curtis and Kleinfeld, 2009; de Kock and Sakmann, 2009; Fee et al., 1997; O'Connor et al., 2010b), mediated in part by an efference copy-like signal originating in vM1 (Ahrens and Kleinfeld, 2004; O'Connor et al., 2002). Integrating signals related to whisking and whisker deflection might underlie object localization (Curtis and Kleinfeld, 2009; Diamond et al., 2008).

The detailed neural circuits underlying the vS1 ↔ vM1 loop are poorly understood. A circuit diagram, based on functional connections between defined cell types, might reveal the primary loci where sensorimotor associations are formed. In addition to the connectivity between cell types, the interactions between neurons in vS1 and vM1 depend on the locations of synapses within the dendritic arbors of the postsynaptic neurons (Larkum et al., 2004; London and Häusser, 2005). Anatomical methods, relying on visualizing axons and dendrites with light microscopy, have often been used to predict circuits (Binzegger et al., 2004; Meyer et al., 2010a; Shepherd et al., 2005). However, axodendritic overlap is not necessarily a good predictor of functional connection strength (Callaway, 2002; Dantzker and Callaway, 2000; Petreanu et al., 2009; Shepherd et al., 2005; White, 2002). Alternatively, electrophysiological methods that detect functional synapses, including paired recordings and glutamate uncaging-based methods, have been applied to map local circuits within vS1 (Bureau et al., 2006; Hooks et al., 2011; Lefort et al., 2009; Lübke and Feldmeyer, 2007; Schubert et al., 2003, 2006; Shepherd et al., 2003, 2005; Shepherd and Svoboda, 2005) and vM1 (Hooks et al., 2011). These techniques require the preservation of pre- and postsynaptic neurons and their axonal processes within a brain slice and are thus mostly limited to local circuits (Luo et al., 2008).

Although a subset of long-range connections between vS1 and vM1 can be preserved in brain slices (Rocco and Brumberg, 2007), it is unclear how complete the preserved circuit is. We previously applied subcellular Channelrhodopsin-2-assisted circuit mapping (sCRACM) to chart the connections made by long-range projections onto vS1 neurons (Petreanu et al., 2009). sCRACM measures connections between presynaptic neurons, defined by ChR2 expression, and postsynaptic neurons, defined by whole-cell recordings. sCRACM relies on photostimulating axons, which can be efficiently excited even when severed from their parent somata. Therefore, sCRACM can map connections between defined neuronal populations over long length scales, not limited to circuits preserved in brain slices. sCRACM also provides an estimate of the spatial distribution of synapses made by ChR2-positive axons onto the dendritic arbors of recorded neurons.

Here, we applied anatomical methods and sCRACM to map inputs from vS1 onto neurons in vM1. vM1 neurons in upper layers (L2/3 and L5A), which harbor mostly cortico-cortical neurons, receive strong input from vS1. These neurons also provide the majority of the projection back to vS1. In contrast, deep layer neurons (L5B and L6), which include the “cortico-fugal” neurons that project to motor centers in the brainstem and elsewhere, received only weak input from vS1.

RESULTS

Reciprocal Connections between vS1 and vM1

We characterized the projections between vibrissal somatosensory cortex (vS1) and vibrissal motor cortex (vM1) using viral-mediated anterograde tracing (Figure 1; see Figure S1 and Movie S1 available online). vS1 was identified by the presence of large barrels. vS1 layers were defined according to well-established cytoarchitectural criteria (Bureau et al., 2006; Groh et al., 2010). Individual layers contain distinct sets of neurons, with different projection patterns and inputs (Groh et al., 2010; Hattox and Nelson, 2007; Sato and Svoboda, 2010; Svoboda et al., 2010).

We labeled vS1 neurons by infection with recombinant adeno-associated viruses (AAV) (Chamberlin et al., 1998) expressing eGFP or tdTomato, and imaged the projections of the infected neurons throughout the brain using a high-resolution slide scanner (excluding most of brainstem and spinal cord). Infected neurons were distributed over several barrel columns (diameter of infection site <1.5 mm) (Figures 1A and 1B), mainly in L2/3 and L5 (Figure S1A). Axonal projections were seen in multiple cortical and subcortical targets. We quantified these projections by integrating the fluorescence intensity over the sections containing specific targets and fluorescent axons (see Supplemental Experimental Procedures). The projections from anatomically strongest to weakest (annotations refer to Paxinos and Franklin [2004]) were as follows: striatum (Str), secondary somatosensory cortex (S2), vM1 (including frontal association cortex [FrA]), thalamic nuclei (Th) (including, posterior thalamic nucleus [PO], reticular thalamic nucleus [RT], and ventral posteromedial thalamic nucleus [VPM]), superior colliculus (SC), ectorhinal/perirhinal cortex (Ect), contralateral vS1, zona inserta (ZI), primary sensory cortical region medial to vS1 (MS1), anterior pretectal nucleus (APT), contralateral Ect, contralateral MS1, re-

uniens thalamic nucleus (Re)/rhomboid thalamic nucleus (Rh), orbital cortex (OC), lateral parietal association cortex (LPtA), infralimbic cortex (IL)/dorsal peduncular cortex (DP) (Figures 1B2, 1B3, 1C and S1B–S1H; see Experimental Procedures and Supplemental Experimental Procedures). These data are qualitatively consistent with previous tracer studies (Fabri and Burton, 1991; Hoffer et al., 2003, 2005; Hoogland et al., 1987; Welker et al., 1988; White and DeAmicis, 1977) but also include projections that have not been reported (e.g., Re/Rh, OC and IL/DP), and poorly characterized medial parietal cortical areas, including MS1 and LPtA.

One of the most prominent projections was vS1 → vM1. Stimulating the vS1-projection zone in vM1 in vivo, using microelectrodes (Donoghue and Parham, 1983; Ferezou et al., 2007; Li and Waters, 1991; Matyas et al., 2010; Porter and White, 1983) or ChR2 photostimulation (Hooks et al., 2011; Matyas et al., 2010), causes whisker protractions at low stimulus intensities (Figure S2). Simultaneous tracing with two viruses expressing different fluorescence proteins (GFP or tdTomato) revealed that the vS1 projection to vM1 and S2 were topographic (Figures 1D, 1E, and S3). The projection zone in vM1 shifted primarily in the anterior-lateral direction as the site of labeling in vS1 moved along a whisker row across arcs (Figure 1E3), in agreement with previous studies in mouse (Welker et al., 1988) and rat (Hoffer et al., 2005). The distance separating the injection sites was 1.5 fold larger than the distance between projection sites (Figure S3H). The vS1 projection split into multiple distinct domains in vM1, offset in the anterior-posterior direction (Figure 1E3, arrowheads).

Apart from the boundary between layer 1 (L1) and layer 2 (L2), vM1 cytoarchitecture is relatively indistinct (Figures 2A and S4), and approaches for defining layers in the motor cortex vary across studies (Brecht et al., 2004; Hooks et al., 2011; Weiler et al., 2008). Here, we defined vM1 layers using a combination of cytoarchitectural criteria and retrograde labeling of neurons by injecting fluorescent microbeads into the vM1 projection zones (Figures 2 and S4). L1 has few neurons. L5A and L2/3 contain high densities of vS1-projecting neurons (Figures 2B and 2C). L5A corresponds to a light zone in bright field images, continuous with L5A of sensory cortex (Weiler et al., 2008). Compared to vS1, L5A in vM1 is relatively superficial (Figure S4). As an agranular cortex, vM1 lacks a clearly defined layer 4 (L4). However, we note that a distinct band between L5A and L2/3 contains neurons that were not labeled by any of the retrograde labeling experiments (Figure 2C, dashed line separating L2/3 and L5A; Anderson et al., 2010). This layer, therefore, appears to harbor mainly local neurons, similar to L4 in sensory cortex. This band also overlaps with L4 markers, such as RAR-related orphan receptor beta (mouse.brain-map.org) (Hooks et al., 2011). However, in terms of its inputs, this band is not obviously different from L2/3 and L5A and was therefore subsumed into these layers for the analysis below. L5A separates L2/3 and deeper layers (5B and 6). Layer 5B (L5B) is defined by the presence of pyramidal tract (PT) type neurons projecting to subcortical targets, including the brainstem and other areas (Figure 2C). In bright field images, layer 6 (L6) appears darker than L5B (Figure 2A). The L5B/L6 boundary corresponds to the lower extent of brainstem-projecting PT type neurons (Figure 2C). L6 has a high density of neurons projecting to the thalamus (Figure 2C).

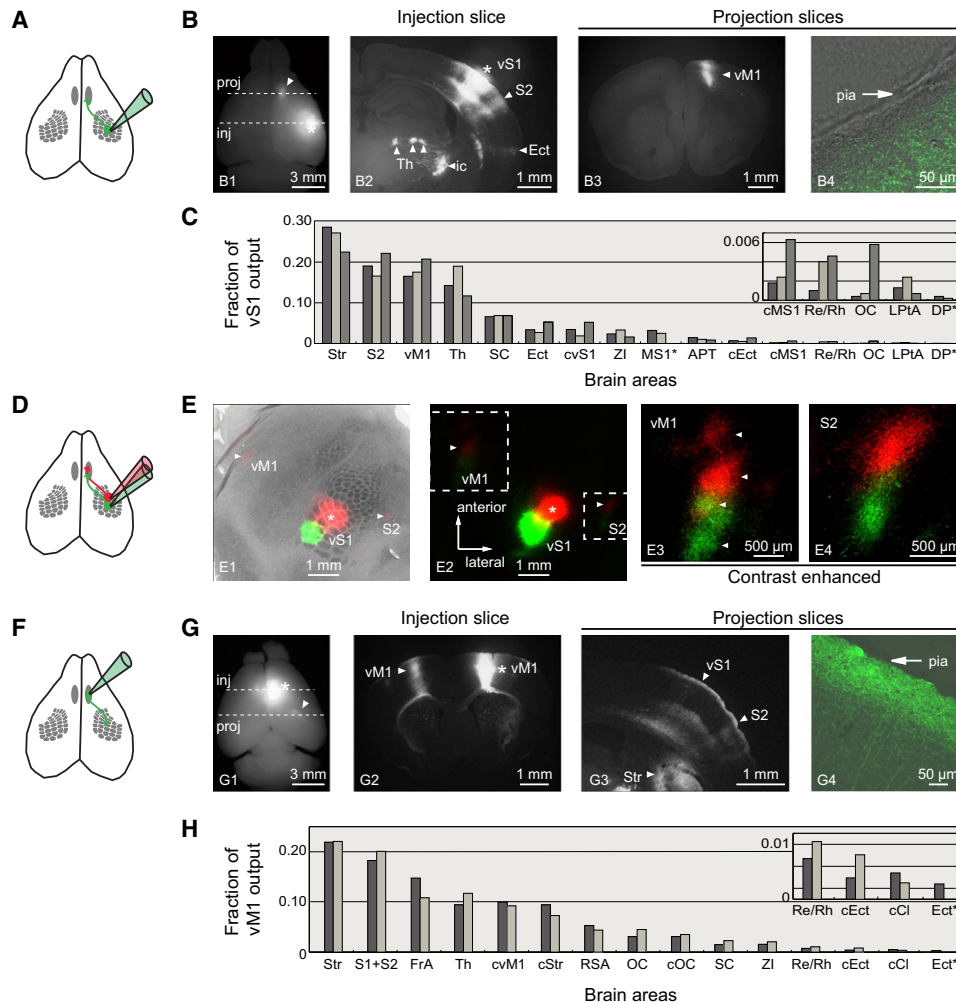


Figure 1. Mapping Output from Somatosensory Cortex (Barrel Cortex, vS1) and Vibrissal Motor Cortex (vM1)

(A–C) Viral injections in vS1 and projections to vM1 and other targets. (A) Schematic, injection in vS1 and projection to vM1. (B) Representative images of injections in vS1 and projections to vM1 and other targets. (B1) AAV-tdTomato injected into vS1 (asterisks) and projection to vM1 (arrowhead). Dashed lines correspond to the sections containing the injection site in vS1 (inj) and the projection site in vM1 (proj). (B2) Coronal section through the vS1 injection site (asterisk). Also shown are projections to second somatosensory cortex (S2), thalamus (Th), and ectorhinal/perirhinal cortex (Ect), and fibers passing through the internal capsule (ic). (B3) Coronal section through vM1. (B4) Confocal image of vS1 axons in vM1, overlaid with a bright field image of the brain slice. (C) Fraction of vS1 output to various brain areas, rank-ordered by strength (quantified based on fluorescence; three separate experiments).

(D and E) Topographic projections from vS1 to vM1 and S2. (D) Schematic, pairs of injections in vS1 and projections to vM1. (E1) AAV-eGFP and AAV-tdTomato injected in nearby parts of vS1 (green, centered on barrel C2; red, centered on barrel C5) (additional examples in Figure S3). The fluorescence image is from a section of flattened cortex, overlaid on a brightfield image showing the cytochrome oxidase stained section to highlight barrels (see Experimental Procedures). (E2) Locations of the projections to vM1 and S2 (dashed boxes). (E3) Contrast-enhanced image showing projections to vM1 (arrowheads indicate split projection). (E4) Contrast-enhanced image showing projections to S2.

(F–H) Projections from vM1 to vS1 and other targets. (F) Schematic, injection in vM1 and projection to vS1. (G1) AAV-eGFP injected into vM1 (asterisks) and projection to vS1 (arrowhead). Dashed lines correspond to the sections containing the injection site in vM1 (inj) and the projection site in vS1 (proj). (G2) Coronal section through the injection site (asterisk) and projection to contralateral vM1. (G3) Coronal section showing vS1, S2, and dorsal lateral striatum (Str). (G4) Confocal image showing vM1 axons in vS1. (H) Fraction of vM1 output to various brain areas, rank-ordered by strength (quantified based on fluorescence; two separate experiments).

Str, striatum; S2, secondary somatosensory cortex; vM1, primary motor, and some area of FrA; Th, thalamus, including PO, Rt, and VPM in (C) and PO, VA, VL in (H); SC, superior colliculus; Ect, ectorhinal/perirhinal cortex; cvS1, contralateral vS1; ZI, zona incerta; MS1, medial primary sensory cortex, medial to vS1 (also see Figure S1); APT, anterior pretectal nucleus; cEct, contralateral side of ectorhinal/perirhinal cortex; cMS1, contralateral side of medial primary sensory cortex; LPtA, lateral parietal association cortex (see Figure S1); OC, orbital cortex; Re/Rh, both ipsilateral and contralateral sides of reuniens thalamic nucleus and rhomboid thalamic nucleus; DP, infralimbic cortex/dorsal peduncular cortex. S1+S2, primary sensory cortex and also including some of secondary sensory cortex; FrA, frontal associate cortex, also might include some intra-vM1 axons; cvM1, contralateral side of primary motor, and contralateral side of FrA; cStr, contralateral side of striatum; RSA, retrosplenial agranular cortex; cOC, contralateral orbital cortex; cCl, contralateral side of claustrum; *one animal's data not shown, either because projections could not be clearly segregated from injection site (for MS1 in C) or not visible (for DP in C), or slightly damaged (for Ect in H). Unless explicitly stated, the region of interest is on the same side as the viral infection. See also Figures S1–S4, Table S1, and Movie S1.

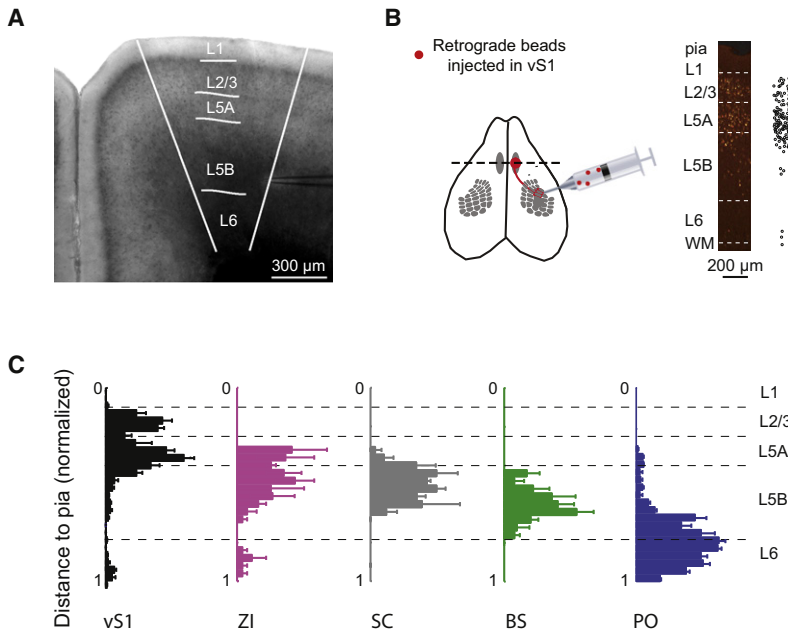


Figure 2. Relationship between Laminar Location and Projection Targets in vM1

(A) Bright field image of a vM1 brain slice. The vertical lines demarcate the recording locations. Horizontal lines indicate layer boundaries.

(B) A representative retrograde labeling experiment. Fluorescent microbeads were injected in vS1 and imaged in vM1.

(C) Fluorescent microbeads were injected in brain areas that are targets of vM1 projections. vS1, black; zona inserta, ZI, magenta; superior colliculus, SC, gray; brainstem, BS, green; posterior thalamic nucleus, PO, blue; three separate experiments for each target brain region; 15 experiments total. Bead-positive cells were mapped and their density plotted against the relative cortical depth (see Experimental Procedures). Error bars, SEM. See also Figures S4 and S5 and Table S1.

across layers in vM1. AAV virus was used to express ChR2 tagged with fluorescent proteins (Nagel et al., 2003) (Venus [Petreanu et al., 2009] or tdTomato) in vS1. In brain slices we recorded from vM1 pyramidal neurons with dendrites overlapping vS1 axons (Figures 3A and S4A).

The deeper layers (L5B and L6) occupy more than half of the depth of vM1. As additional data on local circuits becomes available, these layers may have to be subdivided further (Anderson et al., 2010; Hooks et al., 2011).

In vM1, a band of vS1 axons ascended from the white matter through most layers (Figure 1B3). Although vS1 axons arborized in L1, they were excluded from the top-most ~20 μm (Figure 1B4), indicating that L1 in vM1 contains sublaminae that participate in distinct circuits. Retrograde labeling experiments revealed that these axons arise mainly from L2/3 and L5A in vS1 (Figures S5A–S5B; Sato and Svoboda, 2010).

We next mapped the output from vM1 (Figures 1F–1H). A cluster (diameter <1.5 mm) of neurons was infected throughout the cortical layers in vM1 (Figure S1A). The projections (from anatomically strongest to weakest) were as follows (Figure 1H): Str, somatosensory cortex (including vS1 and S2), FrA (including projections within vM1), Th (including PO, ventral-antero/ventral-lateral thalamic nucleus [VA/VL], and VPM), contralateral vM1, contralateral Str, retrosplenial agranular cortex (RSA), OC, contralateral OC, SC, ZI, Re/Rh, contralateral Ect (cEct), contralateral claustrum (cCl), and Ect (Figures 1G1–1G3, 1H, and S1I–S1K; Experimental Procedures and Supplemental Experimental Procedures; Miyashita et al., 1994; Porter and White, 1983). A prominent projection was vM1 → vS1. In vS1, vM1 axons ascended from the white matter and arborized in L5 and, most abundantly, in L1 (Figures 1G3 and 1G4; Cauler et al., 1998; Petreanu et al., 2009; Veinante and Deschênes, 2003). These observations confirm that vS1 and vM1 are strongly connected in a reciprocal manner in mice.

ChR2-Based Mapping of Long-Range Neuronal Connections

We used subcellular ChR2-assisted circuit mapping (sCRACM) to measure the strength of input from vS1 to excitatory neurons

In most experiments (except in Figures 6B, S6F, S8B, and S8C) the bath contained TTX (1 μM), to eliminate action potentials, and 4-AP (100 μM), to block the K⁺ channels that are critical for repolarizing the axon (Petreanu et al., 2009). Under these conditions short laser pulses (1–2 ms) depolarized ChR2-expressing axons in the vicinity of the laser beam and triggered the local release of glutamate. CPP (5 μM) was added to the bath to block nonlinear NMDA conductances in the postsynaptic dendrites. Measurements of postsynaptic currents (EPSC_{sCRACM}) then revealed the presence of functional synapses between ChR2-expressing axons and the recorded neuron in the vicinity (<60 μm) of the photostimulus (Petreanu et al., 2009). Block of action potentials also prevented possible contributions from polysynaptic pathways.

Stimuli were delivered on a grid pattern which covered the entire dendritic arbor of the recorded cell (Figures 3A and 3B). Maps were reproducible across iterations (repeated 2–4 times; Figure 3C). Averaged EPSC_{sCRACM} were used as pixel values in sCRACM input maps (Figure 3D). Aligning the dendritic arbor of the recorded cell with sCRACM maps revealed the dendritic locations where the synapses from ChR2-positive axons occurred. Because of electrotonic filtering more distant inputs are relatively more attenuated, and sCRACM maps represent a soma-centric view of the spatial distribution of synaptic input within the recorded neurons (Petreanu et al., 2009). Multiple neurons were recorded sequentially in the same brain slice (lateral distances <300 μm, with overlapping dendrites), under identical conditions (Figure 3D). Within-slice comparisons of input strength are necessary because ChR2 expression varies across experiments.

The Strength of vS1 Input as a Function of Cortical Layer

We compared the strength of vS1 input to pyramidal neurons in different layers in vM1 (Figure 4). We summed pixels with

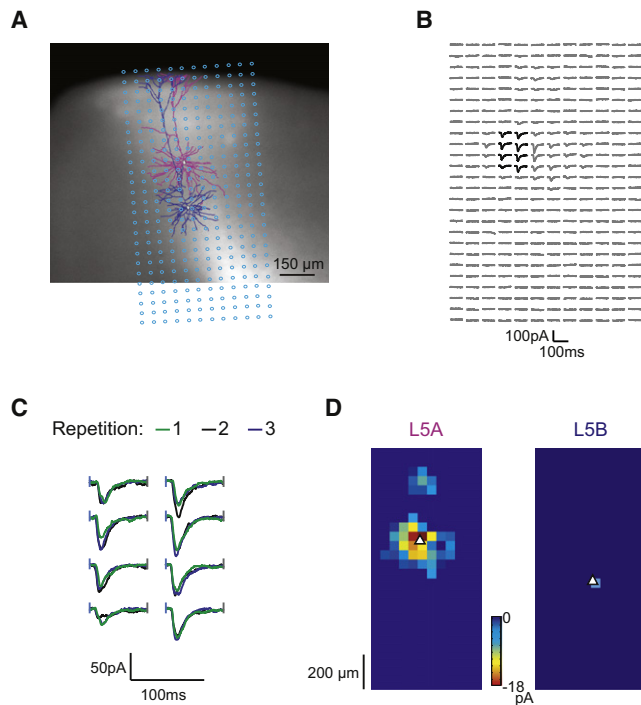


Figure 3. Subcellular Channelrhodopsin-2-Assisted Circuit Mapping (sCRACM)

(A) A vM1 slice overlaid with the photostimulation grid (12 × 26, 50 μ m spacing) and the reconstructed dendrites of two sequentially recorded cells (L5A, magenta; L5B, blue) in the same column of the same slice. White fluorescence, vS1 axons.

(B) Excitatory postsynaptic currents (EPSC_{sCRACM}) recorded from the L5A cell (magenta in A), evoked by photostimulation on a grid (black traces are reproduced at higher magnification in C). EPSC_{sCRACM} are caused by local depolarization of ChR2-positive axons, triggered by blue light.

(C) EPSC_{sCRACM} were reproducible across repetitions (three repetitions; photostimulus locations as for black traces in B). Blue ticks indicate the photostimuli. The blue and gray ticks demarcate the window for calculating the response plotted in sCRACM input maps.

(D) sCRACM input maps. Left panel, L5A cell in (A). Right panel, L5B cell in (A). The pixel value is proportional to the strength of input from ChR2-positive axons to particular locations of the dendritic arbor. The triangles indicate the soma locations. Two maps were obtained under the same stimulation and recording conditions.

See also Figures S4 and S5.

significant responses (>6 \times standard deviation) to estimate input strength (Figures 4C–4F; other analyses without thresholding produced similar results; Figures S6D–S6I; also see Experimental Procedures).

For all cells we compared the input strength to that of L5A neurons, which received the strongest input from vS1. L2/3 neurons received similarly strong input (Figure 4C; $p > 0.5$, signed-rank test). In experiments where input was detected in one L5A cell (failures did occur in a small fraction of experiments due to insufficient ChR2 expression), other L2/3 and L5A cells also showed input. This suggests that most, perhaps all, L2/3 and L5A cells in the vS1 projection zone within vM1 receive input from vS1.

In contrast to the upper layer neurons, many (but not all) L5B and L6 cells did not receive detectable vS1 input. Input to large pyramidal neurons in L5B was 7-fold weaker than input to L5A cells on average ($p < 0.001$, signed-rank test); input to L6 was 10-fold weaker than input to L5A ($p < 0.001$, signed-rank test). Together, these data show that the laminar location of the soma is a key determinant of the strength of input from vS1. L5A and L2/3 neurons, containing mostly cortico-cortical and local cortical neurons, receive strong input from vS1. L5B and L6, containing the vast majority of vM1 neurons projecting out of the cortex, receive relatively little direct input from vS1.

The Distribution of vS1 Input within the Dendrites of vM1 Neurons

We next analyzed the spatial distribution of vS1 input within the dendritic arbors of vM1 neurons. sCRACM input maps were averaged, aligned either on the pia (Figure 5A) or the soma (Figure 5B). Since the density of ChR2-positive axons varies between preparations, the measured vS1 input varied greatly across experiments. Therefore, individual sCRACM maps were normalized before averaging, by dividing with the largest pixel in a map. The average maps thus represent the relative distribution of input within the dendritic tree. L2/3 neurons received input within a single, contiguous domain, centered on the soma, approximately 50 μ m above the peak of basal dendrite length density (Figure 5B1). Input to L5A neurons was split into separate basal and apical domains. The basal domain was centered on the basal dendrites, whereas the apical domain was on the border between L1 and L2. When it was present, the input to L5B neurons was primarily in the basal dendrites. Input to L6 neurons was mainly on the proximal apical dendrites. These spatial distributions of input were also apparent in individual maps (Figure S6A). In general, regions with large input corresponded to high densities of dendritic length (Figure 5B). But there were exceptions to this rule; for example, input to L6 targeted proximal apical dendrites, avoiding the denser basal dendrites (Figure 5B4). These findings indicate that input from vS1 targets specific domains within the dendritic arbors of vM1 neurons.

The Strength of vS1 Input to PT Type Neurons

PT type neurons project to the brainstem reticular formation, the facial nucleus and the spinal trigeminal nucleus (Grinevich et al., 2005; Hattox et al., 2002; Miyashita et al., 1994). These neurons are located in L5B, intermingled with pyramidal neurons projecting to other targets (Nudo and Masterton, 1990) (Figures 2C, S5C, and S5D). Although L5B neurons received weak vS1 input on average (Figure 4D), a small fraction of cells received strong input from vS1 (Figures 6A and S6). These outliers were not necessarily near the L5A/L5B border (Figure S6B). We thus wondered if L5B cells with large vS1 input might correspond to PT type neurons projecting to brainstem. To test this possibility, we injected ChR2 into vS1 and fluorescent microbeads into the reticular formation and facial nucleus. In vM1 slices we recorded from bead-labeled cells in L5B and unlabeled neurons in L2/3 and L5A in the same column. Responses in bead-labeled neurons were small compared to upper layer neurons ($p < 0.001$, signed-rank test), and indistinguishable

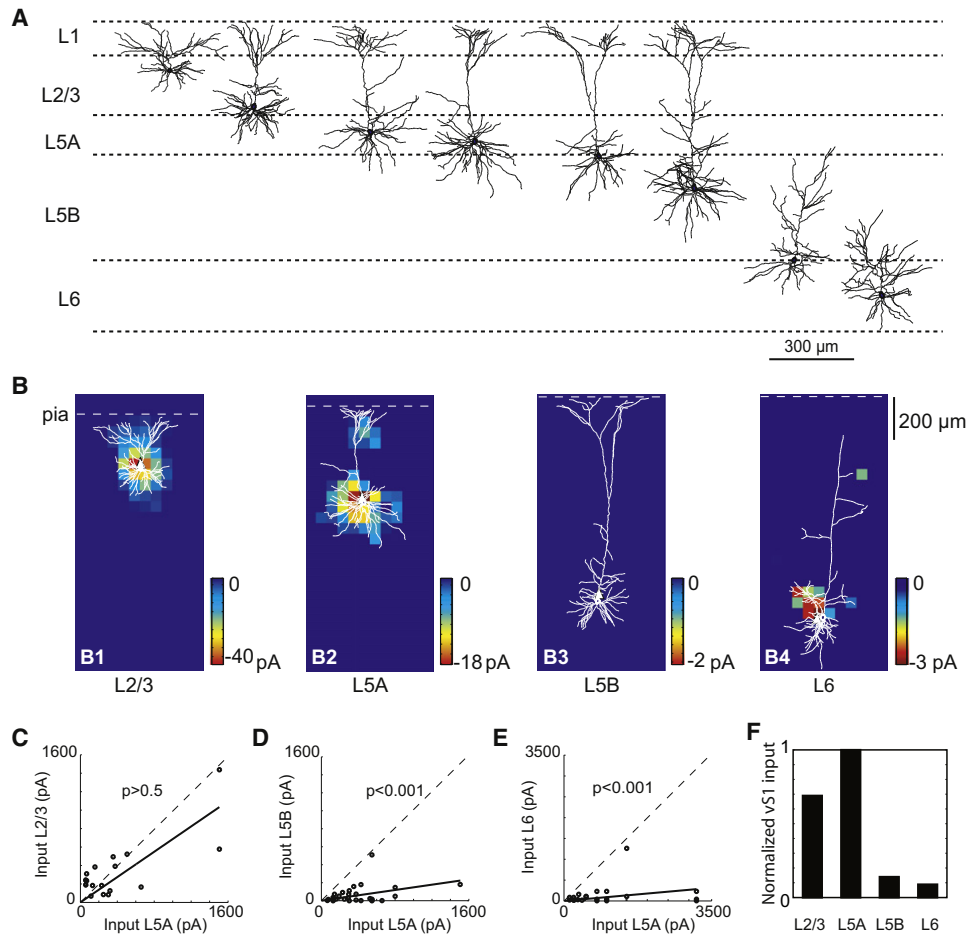


Figure 4. Input from vS1 to vM1 as a Function of Layer

(A) Representative dendritic arbors in vM1, sorted by depth in the cortex.

(B) sCRACM input maps in different layers. The maps were thresholded to show pixels with significant signal (Experimental Procedures). Note differences in color scales.

(C–E) Comparison of input using L5A as the reference. A neuron in L2/3 (C) ($n = 19$ pairs of cells, 11 mice), L5B (D) ($n = 31$ pairs of cells, 15 mice), or L6 (E) ($n = 21$ pairs of cells, 8 mice) neurons is plotted against input to L5A neurons. Statistics, signed-rank test.

(F) Summary of pair wise comparisons. The histogram corresponds to the slopes of the regression lines in (C)–(E).

See also Figure S6 and Table S1.

from unlabeled L5B neurons ($p > 0.1$, ranksum test) (Figures 6C, 6D, S6E, and S6H).

Large pyramidal neurons have electrotonically complex structure (Johnston et al., 1996; London and Häusser, 2005). Distal inputs are filtered and may rely on non-linear mechanisms for amplification. We considered the possibility that detecting vS1 input at the soma of large L5B neurons might require functional NMDA-Rs (Larkum et al., 2009), sodium channels (Magee and Johnston, 1995), or calcium channels (Helmchen et al., 1999). We recorded ChR2-photostimulation-evoked postsynaptic potentials with these channels intact (omitting TTX, CPP, and 4-AP from the bath) (Figures 6B and S6F). These measurements were consistent with the sCRACM measurements. ChR2-photostimulation-evoked responses were 6–7 times weaker in L5B neurons compared to upper layer neurons recorded under iden-

tical conditions ($p < 0.001$, signed-rank test). The shapes of the input maps were different under the two conditions, because, in the absence of TTX, action potential propagation delocalizes the effects of photostimulation (Petreanu et al., 2007, 2009). These results support the conclusion that L5B cells, including PT type neurons, receive little input from vS1 compared to superficial vM1 neurons.

We note that the differences in vS1 input strength to L5B and upper layer cells (L2/3, L5A) cannot be explained by the overlap between vS1 axons and vM1 dendrites. Indeed, L5A neurons received significantly more input from vS1 than L5B neurons, even when normalized for dendritic length density (Figure S7). Similar types of specificity have been reported in projections from the thalamic PO nucleus to vS1 (Petreanu et al., 2009). For comparison we provide this data (Figure S8). This confirms

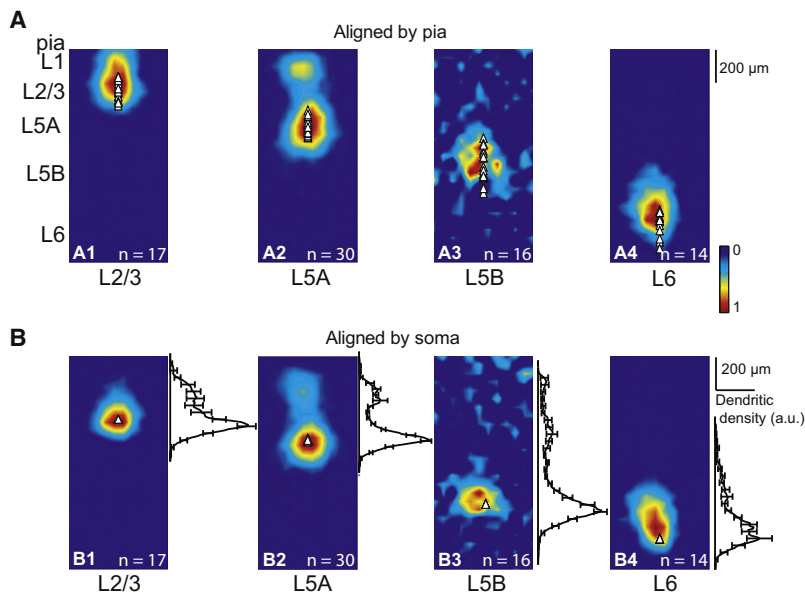


Figure 5. Laminar Input to vM1 Neurons from vS1

(A) Averaged sCRACM input maps aligned by pia. Triangles, soma locations (number of cells in each group are noted in each panel; total $n = 77$ cells, 35 mice).

(B) Averaged sCRACM input maps aligned by soma locations. Right, averaged dendritic length density as a function of depth in the cortex (dendritic reconstructions were performed for a subset of cells; L2/3, $n = 7$; L5A, $n = 19$; L5B, $n = 15$; L6, $n = 5$). The integral of the dendritic density was normalized to 1.

See also Figure S6 and Table S1.

that geometric overlap is not an accurate predictor of the strengths of functional projections (Brown and Hestrin, 2009; Callaway, 2002; Shepherd et al., 2005).

vS1-Projecting Neurons in vM1 Receive Input from vS1

L2/3 and L5A neurons in vS1 provide input to L2/3 and L5A neurons in vM1 (Figures S5A, S5B, and S9; Sato and Svoboda, 2010). Similarly, a subset of vM1 neurons, concentrated in L2/3 and L5A, connect with L2/3, L5A, and L5B neurons in vS1 (Petreanu et al., 2009; Figures 2B and 2C). Do neurons in L2/3 and L5A in vS1 and vM1 form a direct feedback loop? Or do L2/3 and L5A in vM1 harbor distinct set of neurons, one receiving input from vS1, and the other sending output to vS1? To directly distinguish between these possibilities we coinjected virus expressing ChR2-venus and retrogradely-transported microbeads into vS1 (Figure 7A). In vM1, the distribution of retrogradely labeled cells overlapped with the band of axonal labeling (Figure 7B). The vast majority of bead-positive cells were located in L2/3 and L5A (Figure 2C), similar to the neurons receiving strong input from vS1 (Figure 4). We measured sCRACM maps for bead-positive cells and neighboring bead-negative cells (soma distance $< 50 \mu\text{m}$, without bias in vertical depth; Figures 7C–7E, S6G, and S6I). Bead-positive vS1-projecting neurons received significantly stronger (2.5-fold) input from vS1 than bead-negative neurons (Figures 7E; $p < 0.001$, signed-rank test). Some bead-positive cells were found (Figure 2C) and recorded in L5B (Figure S6C). Similar to bead-positive cells in L2/3 and L5A, bead-positive cells in L5B received stronger vS1 input comparable to neighboring bead-negative cells (sub group in Figure 7E; $p < 0.001$, signed-rank test); but the input was still much less than the input to upper layer cells in the same column (Figure S6I; $p < 0.001$, signed-rank test). We also performed the converse experiments, recording in vS1 from vM1-projecting neurons and their neighbors (Figure S9). Here, there was no difference between bead-positive and bead-negative neurons (Figure S9G; $p > 0.1$, signed-rank test). Thus, neurons in upper layers (L2/3 and L5A)

of vS1 and vM1 form a strong feedback loop. Furthermore, within a layer, a neuron's projection pattern can determine the strength of specific types of input.

DISCUSSION

We used viral anterograde tracing, retrograde labeling, and Channelrhodopsin-2-assisted circuit mapping to describe the circuits linking vS1 (barrel cortex) and pyramidal neurons in vM1 (vibrissal motor cortex). vS1 axons preferentially targeted upper layer (L2/3, L5A) neurons in vM1 (Figure 4). vM1 neurons projecting back to vS1 received particularly strong direct input from vS1 (Figure 7). vS1 input to neurons in deeper layers (L5B, L6) was weak (Figure 4). vS1 input conspicuously avoided the majority of pyramidal tract (PT) type neurons (Figure 6), despite pronounced overlap of dendrites and axons. Our findings suggest that upper layers in vM1 participate in forming sensorimotor associations (Figure 8).

AAV-Mediated Anterograde Tracing

For anterograde tracing we used AAV expressing GFP or the red fluorescent protein tdTomato (Shaner et al., 2004) to infect neurons in vS1 or vM1 (Figures 1 and S1; Movie S1). A high-resolution slide scanner was used to image fluorescent axons throughout the brain (Supplemental Experimental Procedures). Expression of the fluorescent proteins produced sufficient contrast to detect and image individual axons in their projection zones (Figures S1D and S1H), often millimeters from their parent cell bodies (Aronoff et al., 2010; De Paola et al., 2006; Grinevich et al., 2005; Petreanu et al., 2009; Stettler et al., 2006). This is remarkable because these axons are the smallest structures in the brain, often with diameters less than 100 nm (Shepherd and Harris, 1998; De Paola et al., 2006). These images allowed us to quantify the projection strength from vS1 and vM1 to numerous areas throughout the brain. We confirmed previously reported projections from the barrel cortex (for example, vS1 \rightarrow striatum, vM1, FrA, thalamus, S2), but we also found projections to other areas (vS1 \rightarrow orbital cortex, reuniens thalamic nucleus/rhomboid thalamic nucleus, infralimbic cortex/dorsal peduncular cortex, MS1, cMS1, LPtA). From the vibrissal motor cortex strong projections included, vM1 \rightarrow striatum, vS1, FrA, thalamus, contralateral vM1. Weaker projections included vM1 \rightarrow contralateral claustrum, which was previously described in rats (Alloway et al., 2009). Quantification of the projection strength

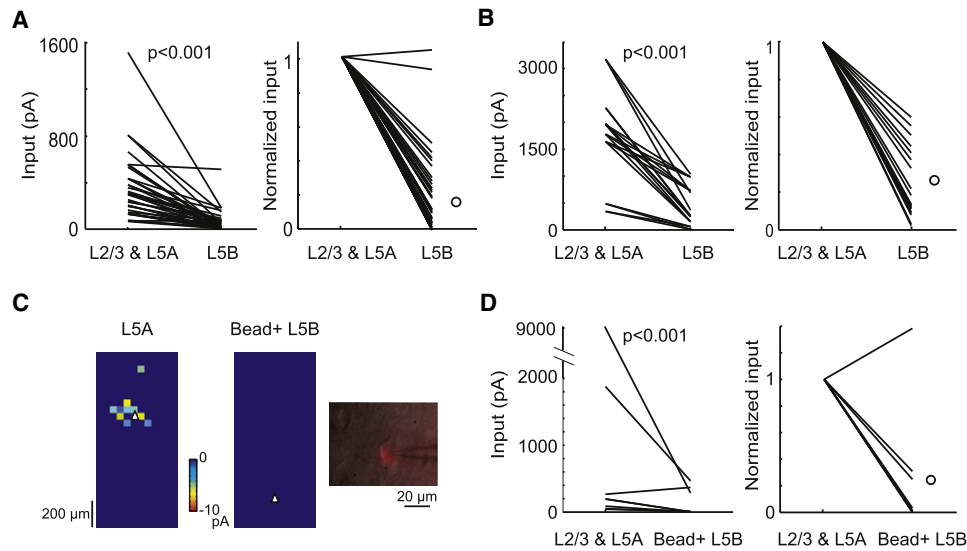


Figure 6. Low Input to Brainstem-Projecting L5B Pyramidal Neurons from vS1

(A) Input to upper layer neurons (L2/3 and L5A) compared to L5B neurons (left, actual values; right, normalized) ($n = 36$ pairs of cells, 17 mice). Statistics, signed-rank test. The circle in the right panel indicates the mean (0.18).

(B) Same experiments as (A), except without antagonist cocktails (CPP, TTX, and 4-AP) ($n = 23$ pairs of cells, 4 mice). Statistics, signed-rank test. The circle in the right panel indicates the mean (0.26).

(C and D) Input to upper layer neurons (L2/3 and L5A) compared to brainstem-projecting L5B neurons. (C) Individual maps of a L5A cell (left) and a bead-positive L5B cell (middle). Triangles indicate the soma locations. Both maps were obtained under identical experimental conditions in the same brain slice. An overlay of DIC and red fluorescence shows a bead-positive L5B cell (right). (D) Input to upper layer neurons (L2/3 and L5A) compared to bead-positive L5B neurons.

(left, actual values; right, normalized) ($n = 8$ pairs of cells, 5 mice). Statistics, signed-rank test. The circle in the right panel indicates the mean (0.28).

See also Figures S5–S8 and Table S1.

based on the total brightness of the projection to particular structures (Figures 1C and 1H) serves to rank-order brain areas for potential importance in vibrissa-dependent somatosensation and functional follow-up experiments (Luo et al., 2008; O'Connor et al., 2009).

Two caveats deserve discussion. First, our quantification of projection strength is only indirectly related to synaptic output. Fluorescence is proportional to axonal volume and since axonal caliber is constant, also to axonal length density. For cortical axons terminating within cortex bouton density is approximately constant (Anderson et al., 2002), and most axonal length resides in these termination zones; fluorescence is, therefore, expected to be an accurate predictor of bouton number and output strength. However, measurements of bouton densities in other target areas are necessary to strengthen the interpretation of projection strength based on fluorescence measurements. Second, numerically small projections can be functionally prominent, as has been documented for thalamocortical projections to L4 in the sensory cortex (Benshalom and White, 1986; da Costa and Martin, 2009).

Simultaneous tracing with pairs of colors (Figures 1E and S3) confirmed that the vS1 → vM1 projection is topographic (Hoffer et al., 2005; Welker et al., 1988). Furthermore, the projection splits into multiple domains (Figure 1E3). Additional experiments are required to determine if vibrissal motor cortex contains multiple motor maps (Tennant et al., 2011). The more caudal domain overlaps with the posterior-medial domain of the tongue motor cortex (Komiya et al., 2010).

The Circuits Connecting vS1 and vM1

The brain is organized on a number of scales, including individual cells, defined groups of neurons, and brain areas. At the highest level, the hierarchical organization of brain areas has long been a cornerstone in our understanding of the mammalian nervous system (Felleman and Van Essen, 1991; Kleinfeld et al., 1999; Sporns and Kötter, 2004). However, each brain area itself contains multiple cell classes, which are connected into complex local circuits (Binzegger et al., 2004; Hooks et al., 2011; Lefort et al., 2009). Subcellular ChR2-assisted circuit mapping (sCRACM) allows long-range connections between brain areas to be linked to defined neuronal populations within the local circuits (Petreanu et al., 2007, 2009).

sCRACM has limitations. First, the detailed mechanisms driving neurotransmitter release evoked by ChR2 may not be the same as when evoked by action potentials (Zhang and Oertner, 2007). However, our results were quantitatively similar with action potentials blocked or intact (Figure 6), suggesting that ChR2-based mapping provides accurate measurements of relative input strength. Second, synaptic currents recorded at the soma can be greatly attenuated by electrotonic filtering in the dendrites. More distal inputs are therefore underrepresented in a sCRACM map. Third, axonal expression levels of ChR2 typically vary greatly across experiments. Comparison of input strength across different postsynaptic neurons therefore requires normalization of input strength within single experiments.

We mapped the long-range connections between sensory and motor areas involved in whisker-based sensation.

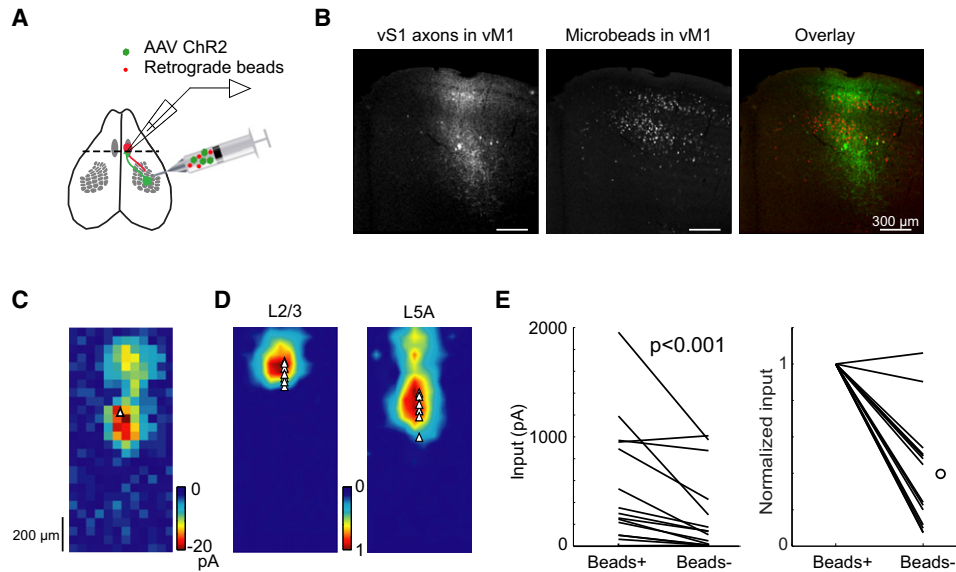


Figure 7. vS1-Projecting Neurons in vM1 Receive Strong Input from vS1

(A) Schematic of the experiment. AAV-ChR2-venus (green) and fluorescent microbeads (red) were coinjected in vS1. Recordings were made in vM1 (dashed line). (B) Representative images of vS1 axons (left), bead-labeled cells (vS1-projecting cells; middle), and the overlay (right) in vM1. (C) Example sCRACM input map recorded in a retrograde bead-positive cell (triangle, soma location). (D) Average sCRACM maps for bead-positive L2/3 neurons (left) aligned on the pia (n = 7 cells, 6 mice) and for bead-positive L5A neurons (right) aligned on the pia (n = 8 cells, 6 mice). (E) Input to bead-positive and nearby (distance < 50 μm) bead-negative cells (left, actual values; right, normalized) (n = 15 pairs of cells, 12 mice). Statistics, signed-rank test. The circle in the right panel indicates the mean (0.40). See also Figures S6 and S9 and Table S1.

Somatosensation relies on active movement of whiskers to gather information in the vicinity of the head. Sensory input is critical for object localization and recognition, and also to guide future movements of the whiskers. By collating our studies of long-range connections with previous data on thalamocortical (Bureau et al., 2006; Lu and Lin, 1993; Meyer et al., 2010b; Petreanu et al., 2009) and local cortical circuits (Hooks et al., 2011; Lefort et al., 2009; Svoboda et al., 2010) it is possible to sketch out a circuit diagram for the cortical vibrissal sensorimotor loop in mice (Figure 8).

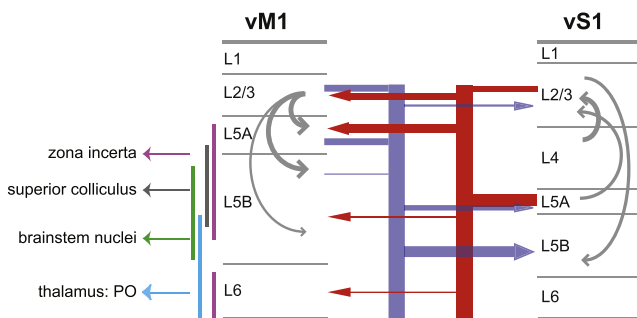


Figure 8. The Long-Range Circuits Connecting vS1 and vM1

Red, projections from vS1 to vM1. Blue, projections from vM1 to vS1. Gray, three strongest intracortical projections. Line thickness is proportional to the strength of connection strength. Targets of vM1 projections: zona incerta (ZI, magenta), superior colliculus (SC, cyan), brainstem (BS, green), and posterior thalamic nucleus (PO, blue).

Forces acting on whiskers excite sensory neurons in the trigeminal ganglion, triggering activity which ascends through the brainstem into VPM and L4 neurons in the barrel cortex (Petersen, 2007; Svoboda et al., 2010). L4 stellate cells mainly excite L2/3 neurons, which in turn excite neurons in L5A and also in L5B (Armstrong-James and Fox, 1987; Brecht et al., 2003; Brecht and Sakmann, 2002; Hooks et al., 2011; Lefort et al., 2009; Manns et al., 2004). A subset of L2/3 and L5A neurons project to vM1 (Figures S5A, S5B, and S9C), where they strongly target upper layer neurons in L2/3 and L5A, and only weakly deep layer neurons in L5B and L6 (Figures 4C–4F, 6, and S6). Upper layer neurons in vM1 receiving strong input from vS1 project back to vS1 (Figures 2B, 2C and 7B), where they synapse onto neurons in L2/3, L5A, and L5B (Petreanu et al., 2009). Cortico-cortical neurons in L2/3 and L5A in vM1 are thus the nexus of a powerful disinaptic feedback loop (vS1, L2/3/5A ↔ vM1, L2/3/5A), linking sensory and motor cortex (Figure 8). This loop apparently violates the no-strong-loops principle which is thought to govern inter-areal connectivity in the visual system (Crick and Koch, 1998).

Since AAV infected both L2/3 and L5A cells in vS1 (Figure S1A), additional experiments are required to determine the separate contributions of L2/3 and L5A neurons to activating targets in vM1 (Aronoff et al., 2010). A small subset of deep L6 cells in vS1 also projected to vM1 (Figures S5A, S5B, and S9C). These neurons were only sparsely infected by the AAV virus, and their contribution to the vS1 → vM1 projection, although likely small in total, was underrepresented in our study.

How does this superficial feedback loop communicate with the deep layer output neurons in vM1? The local circuit in somatic (Weiler et al., 2008) and vibrissal (Hooks et al., 2011) motor cortex shows a top-to-bottom organization. Interlaminar excitation is strongest from superficial layers downward, with a powerful descending projection from L2/3 to the border of L5A and L5B (Hooks et al., 2011). Weaker projections exist from L5A to L5B. Similarly, L2/3 and/or L5A neurons in vM1 excite L5B neurons in vS1 (Petreanu et al., 2009). L5B neurons in vM1 (Figures 2 and S5D) and vS1 (Matyas et al., 2010) are projecting to motor centers in the brainstem. Our studies thus suggest that sensorimotor integration underlying adaptive whisking occurs primarily in the superficial layers, and the results of this computation are then passed on to neurons in deeper layers, which control motor centers (Fetz and Baker, 1973; Matyas et al., 2010).

PT type neurons in L5B of vM1 primarily control whisker protractions, whereas PT type neurons in L5B of vS1 might control whisker retractions (Matyas et al., 2010). Our studies suggest that whisker retractions triggered by intracortical microstimulation in vM1 are mediated by direct stimulation of corticocortical neurons in L2/3 and L5A, which in turn excite deep layers in vS1 (Petreanu et al., 2009).

The documented sources of synaptic input to deep neurons in vM1, including PT type neurons, remain few and weak (Hooks et al., 2011; Anderson et al., 2010; Figures 4 and 6). L5B and L6 neurons receive only weak input from superficial layers (Hooks et al., 2011; Anderson et al., 2010) and from vS1 (Figures 4 and 6). Additional studies of other possible sources of input, including the thalamus and the anterior cortex, will be necessary to account for the input to PT type neurons in vM1.

Specificity in Long-Range Projections

Numerous experiments using a variety of techniques have shown that the overlap of axons and dendrites fails to accurately predict the strengths of connections between neuronal populations (Callaway, 2002; White, 2002). For example, in vS1, L4 neurons strongly excite L2/3 pyramidal cells, but not intermingled somatostatin-positive interneurons (Dantzker and Callaway, 2000). In the rat vS1 but not in the mouse (Bureau et al., 2006), L2/3 pyramidal cells above barrels are strongly excited by L4 neurons, whereas L2/3 pyramidal cells above septa receive only weak input (Shepherd et al., 2003; Shepherd and Svoboda, 2005). In mouse vS1, L5A neurons receive strong input from PO, whereas neighboring large-tufted L5B neurons do not (Petreanu et al., 2009; Figure S8). Similarly, in the mouse vM1, L5A neurons receive strong input from vS1 compared to L5B neurons (Figures 3D, 4B–4F, 6, and S7). Input strength can also depend on the neuron's projection target (Figure 7; Anderson et al., 2010). Specificity beyond structure also exists at the level of subcellular distributions of synapses. For example, L6 neurons in vM1 receive input mainly on their sparse apical dendrite, and little input on their basal dendrites (Figures 4B4 and 5B4). These findings highlight the need for methods of circuit-mapping that detect functional synapses.

Sensorimotor Integration

Mice whisk in an adaptive manner to extract information about the tactile world. For example, in object localization tasks

rodents move their whiskers to locate an object in the vicinity of their heads (Knutsen et al., 2006; Mehta et al., 2007; O'Connor et al., 2010a). Here, a sensory cue (typically visual or auditory) triggers a motor program which leads to contact between whisker and object. The sensory input in turn changes the whisking pattern (Mitchinson et al., 2007; O'Connor et al., 2010a). Ultimately the animal makes a judgment about object location to collect a reward by executing a second motor program involving licking. A standard laboratory task of this type therefore involves multiple stimulus-response associations (Lalazar and Vaadia, 2008). The microcircuitry connecting sensory and motor cortices described here might help to implement these stimulus-response associations.

It has been suggested that vibrissa-based object localization requires the brain to interpret contact between whisker and object in the context of an internal reference signal indicating whisker location or phase (Curtis and Kleinfeld, 2009; Diamond et al., 2008). This reference signal might consist of an efference copy generated by the inverse model driving goal-directed whisking. The circuits uncovered here may underlie mixing of whisking and contact signals and thus, might underlie computation of object location.

EXPERIMENTAL PROCEDURES

Stereotactic Injections

Experiments were conducted according to National Institutes of Health guidelines for animal research and were approved by the Institutional Animal Care and Use Committee at Janelia Farm Research Campus. For anterograde tracing we used adeno-associated virus (AAV; serotype 2/1) expressing eGFP (www.addgene.com) or tdTomato (a gift from J. Magee) under the CAG promoter. For sCRACM mapping experiments, we used AAV virus (serotype 2/1; in some experiments serotype 2/10) expressing either ChR2-venus (Petreanu et al., 2009) or ChR2-tdTomato (www.addgene.com). For retrograde tracing we used fluorescent LumaFluor microbeads (LumaFluor Inc.). C57BL/6J mice (Charles River) (13–16 days old) were anesthetized using an isoflurane-oxygen mixture and placed in a custom stereotactic apparatus. A small hole was drilled into the skull, allowing insertion of a pulled glass pipette (Drummond) (tip diameter: 10–20 μm for virus; 40–60 μm for LumaFluor microbeads). For sCRACM experiments, coordinates were as follows (in mm, from bregma): vS1, 0.5 to 0.8 posterior, 2.9–3.3 lateral; vM1, 1.0–1.1 anterior, 0.60–0.75 lateral. Injections sites were confirmed by post hoc histological analysis (Figures 1B, 3, 4, 5, 6, 7, and S1B–S1H). See Supplemental Experimental Procedures for further details.

Slice Preparation and Electrophysiology

Brain slices were prepared as described (Bureau et al., 2006) 14 to 24 days after viral infections (see Supplemental Experimental Procedures). For vM1, the brain was tilted $\sim 10^\circ$ to 15° forward during slicing to optimize the alignment of apical dendrites with the slice surface. When cutting from rostral to caudal, 1–2 slices, ~ 0.8 – 1.3 mm anterior to bregma, corresponding to the first and/or second slice containing a fused corpus callosum, were used. For vS1 slices, the brain was cut in the coronal plane. Only slices with prominent barrels (Figure S9B) were used (Petreanu et al., 2009).

All recordings were performed at room temperature in circulating ACSF. For most experiments (except Figures 6B, S6F, S8B, and S8C) TTX (1 μM), 4-AP (100 μM), and CPP (5 μM) were added (Petreanu et al., 2009). Whole-cell recordings were obtained using borosilicate pipettes (resistance 4–6 M Ω) and an Axopatch 700B amplifier (Axon Instruments). The intracellular solution contained (in mM): 128 potassium gluconate, 4 MgCl₂, 10 HEPES, 1 EGTA, 4 Na₂ATP, 0.4 Na₂GTP, 10 sodium phosphocreatine, 3 sodium L-ascorbate, and 0.02 Alexa-594 (Molecular Probes), and 3 mg/ml biocytin (pH 7.27; 287 mOsm). Cells were recorded at depths from 46 to 103 μm

within the brain slice. Data were acquired using *Ephus* (www.ephus.org). Pyramidal neurons were selected based on their morphology confirmed under fluorescence microscopy (Alexa-594 in pipette solution) or post hoc by biocytin staining. For sCRACM mapping, EPSC were recorded in voltage clamp while holding at -70 mV (L2/3 cells) or -75 mV (L5 cells). Access resistances ranged 10–40 M Ω . For every vM1 cell included in the data set, the site of viral infection was confirmed to lie within the barrel cortex by post hoc histological analysis. Most infections were roughly centered on the barrel field.

Photostimulation

The position of a blue laser beam (473 nm; Crystal Laser) was controlled with galvanometer scanners (Cambridge Scanning, Inc.). The beam passed through an air objective (4 \times ; 0.16 NA; UPlanApo, Olympus) and was nearly cylindrical (~ 8 – 16 μ m in diameter, full-width at half max at the specimen plane). The light pulses were controlled with a Pockels cell (ConOptics). The power (0.7–1.8 mW) of the light pulses (duration, 1–2 ms) was adjusted so that the largest EPSC_{sCRACM} had peak values in the range of 50–100 pA; in some cases EPSC_{sCRACM} were smaller even at the highest laser powers. Each trial consisted of approximately 100 ms baseline, the photostimulus, and 300 ms response period. Stimulation sites were on a 50 μ m grid. Grid sizes (12 \times 24, 12 \times 26 or 12 \times 28) were adjusted based on the size of the neuron; all grids covered all potential sites of input within the dendritic arbor. Each map was repeated 2–4 times. The laser stimuli were given in a spatial sequence designed to maximize the intervals between stimuli arriving to neighboring spots (Shepherd et al., 2003).

Data Analysis

sCRACM pixel values corresponded to the mean EPSC amplitude in a 75 ms time window after the onset of the stimulus (given in picoamperes, pA, for consistency with previous studies). In some figure panels (Figures 3D and 4B), we display only pixels with significant responses (response amplitude $>6\times$ standard deviation of the baseline). For each cell, maps were averaged across repeats. To show the spatial distribution of input, maps were first peak-normalized (Figures 5, 7D, S9E, and S9F) and then averaged across cells within a class. Normalization was necessary because response amplitudes vary across experiments depending on the infection efficiency and the ChR2 expression level.

To quantify the total input for pairs of neighboring neurons we summed all pixels that showed significant responses ($>6\times$ standard deviation of the baseline; Figures 3D, 4C–4F, 6, 7E, S8D, and S8E). Only cell pairs with some distance ≤ 300 μ m and dendritic overlap were used. We performed additional analyses to check for possible biases imposed by thresholding ($>6\times$ standard deviation of the baseline): First, we computed input across a 3 \times 3 grid around the soma (Figures S6D–S6F). Second, we generated a mask by averaging the responses across cells within a group. The mask was defined by significant responses ($>5\times$ standard deviation). The mask was then used to compute input from the original maps (Figures S6G–S6I). Third, we also computed the mean pixel value over the entire map without thresholding (data not shown). These three analysis methods yielded consistent results. Since the time between stimulus and the beginning of the baseline period for the next trial was fairly short (300 ms), we corrected for bleedthrough across trials (baseline drift). Because the grid size for stimulation was always larger than the dendritic arbors of the recorded cells (for example, Figure 3B), we estimated the baseline drift from the traces far outside the cell's dendritic arbor (these traces were "blanks" that could not have contained true responses; they thus represent pure baseline drift). We then subtracted the baseline drift from the mean value of all other traces.

Paired comparisons used the nonparametric Wilcoxon signed-rank test (Figures 6, 7, S6, S7, and S9).

SUPPLEMENTAL INFORMATION

Supplemental Information includes nine figures, one table, one movie, and supplemental text and can be found with this article online at [doi:10.1016/j.neuron.2011.07.029](https://doi.org/10.1016/j.neuron.2011.07.029).

ACKNOWLEDGMENTS

This work was funded by the Howard Hughes Medical Institute. We thank Gordon Shepherd for advice and extensive discussions; Asaf Keller for advice on electrical microstimulation in vM1; Tim O'Connor for programming; Brenda Shields, Amy Hu, Alma Arnold, and Kevin McGowan for technical support; Takashi Sato and Haining Zhong for help with experiments and analysis; Stefanie Kaech Petrie for help with the blind retrograde beads counting; and Diego Gutnisky and Zengcai Guo for comments on the manuscript.

Accepted: July 29, 2011

Published: October 5, 2011

REFERENCES

- Ahrens, K.F., and Kleinfeld, D. (2004). Current flow in vibrissa motor cortex can phase-lock with exploratory rhythmic whisking in rat. *J. Neurophysiol.* 92, 1700–1707.
- Alloway, K.D., Smith, J.B., Beauchemin, K.J., and Olson, M.L. (2009). Bilateral projections from rat M1 whisker cortex to the neostriatum, thalamus, and claustrum: forebrain circuits for modulating whisking behavior. *J. Comp. Neurol.* 515, 548–564.
- Anderson, J.C., Binzegger, T., Douglas, R.J., and Martin, K.A. (2002). Chance or design? Some specific considerations concerning synaptic boutons in cat visual cortex. *J. Neurocytol.* 31, 211–229.
- Anderson, C.T., Sheets, P.L., Kiritani, T., and Shepherd, G.M. (2010). Sublayer-specific microcircuits of corticospinal and corticostriatal neurons in motor cortex. *Nat. Neurosci.* 13, 739–744.
- Armstrong-James, M., and Fox, K. (1987). Spatiotemporal convergence and divergence in the rat S1 "barrel" cortex. *J. Comp. Neurol.* 263, 265–281.
- Aronoff, R., Matyas, F., Mateo, C., Ciron, C., Schneider, B., and Petersen, C.C. (2010). Long-range connectivity of mouse primary somatosensory barrel cortex. *Eur. J. Neurosci.* 31, 2221–2233.
- Benshalom, G., and White, E.L. (1986). Quantification of thalamocortical synapses with spiny stellate neurons in layer IV of mouse somatosensory cortex. *J. Comp. Neurol.* 253, 303–314.
- Binzegger, T., Douglas, R.J., and Martin, K.A. (2004). A quantitative map of the circuit of cat primary visual cortex. *J. Neurosci.* 24, 8441–8453.
- Brecht, M., and Sakmann, B. (2002). Dynamic representation of whisker deflection by synaptic potentials in spiny stellate and pyramidal cells in the barrels and septa of layer 4 rat somatosensory cortex. *J. Physiol.* 543, 49–70.
- Brecht, M., Roth, A., and Sakmann, B. (2003). Dynamic receptive fields of reconstructed pyramidal cells in layers 3 and 2 of rat somatosensory barrel cortex. *J. Physiol.* 553, 243–265.
- Brecht, M., Krauss, A., Muhammad, S., Sinai-Esfahani, L., Bellanca, S., and Margrie, T.W. (2004). Organization of rat vibrissa motor cortex and adjacent areas according to cytoarchitectonics, microstimulation, and intracellular stimulation of identified cells. *J. Comp. Neurol.* 479, 360–373.
- Brown, S.P., and Hestrin, S. (2009). Intracortical circuits of pyramidal neurons reflect their long-range axonal targets. *Nature* 457, 1133–1136.
- Bureau, I., von Saint Paul, F., and Svoboda, K. (2006). Interdigitated paralemniscal and lemniscal pathways in the mouse barrel cortex. *PLoS Biol.* 4, e382. [10.1371/journal.pbio.0040382](https://doi.org/10.1371/journal.pbio.0040382).
- Callaway, E.M. (2002). Cell type specificity of local cortical connections. *J. Neurocytol.* 31, 231–237.
- Carvell, G.E., and Simons, D.J. (1990). Biometric analyses of vibrissal tactile discrimination in the rat. *J. Neurosci.* 10, 2638–2648.
- Caulier, L.J., Clancy, B., and Connors, B.W. (1998). Backward cortical projections to primary somatosensory cortex in rats extend long horizontal axons in layer I. *J. Comp. Neurol.* 390, 297–310.
- Chakrabarti, S., and Alloway, K.D. (2006). Differential origin of projections from S1 barrel cortex to the whisker representations in SII and M1. *J. Comp. Neurol.* 498, 624–636.

- Chamberlin, N.L., Du, B., de Lacalle, S., and Saper, C.B. (1998). Recombinant adeno-associated virus vector: use for transgene expression and anterograde tract tracing in the CNS. *Brain Res.* 793, 169–175.
- Crick, F., and Koch, C. (1998). Constraints on cortical and thalamic projections: the no-strong-loops hypothesis. *Nature* 391, 245–250.
- Curtis, J.C., and Kleinfeld, D. (2009). Phase-to-rate transformations encode touch in cortical neurons of a scanning sensorimotor system. *Nat. Neurosci.* 12, 492–501.
- da Costa, N.M., and Martin, K.A. (2009). The proportion of synapses formed by the axons of the lateral geniculate nucleus in layer 4 of area 17 of the cat. *J. Comp. Neurol.* 516, 264–276.
- Dantzker, J.L., and Callaway, E.M. (2000). Laminar sources of synaptic input to cortical inhibitory interneurons and pyramidal neurons. *Nat. Neurosci.* 3, 701–707.
- de Kock, C.P.J., and Sakmann, B. (2009). Spiking in primary somatosensory cortex during natural whisking in awake head-restrained rats is cell-type specific. *Proc. Natl. Acad. Sci. USA* 106, 16446–16450.
- De Paola, V., Holtmaat, A., Knott, G., Song, S., Wilbrecht, L., Caroni, P., and Svoboda, K. (2006). Cell type-specific structural plasticity of axonal branches and boutons in the adult neocortex. *Neuron* 49, 861–875.
- Diamond, M.E., von Heimendahl, M., Knutsen, P.M., Kleinfeld, D., and Ahissar, E. (2008). 'Where' and 'what' in the whisker sensorimotor system. *Nat. Rev. Neurosci.* 9, 601–612.
- Donoghue, J.P., and Parham, C. (1983). Afferent connections of the lateral agranular field of the rat motor cortex. *J. Comp. Neurol.* 217, 390–404.
- Fabri, M., and Burton, H. (1991). Ipsilateral cortical connections of primary somatic sensory cortex in rats. *J. Comp. Neurol.* 311, 405–424.
- Farkas, T., Kis, Z., Toldi, J., and Wolff, J.R. (1999). Activation of the primary motor cortex by somatosensory stimulation in adult rats is mediated mainly by associational connections from the somatosensory cortex. *Neuroscience* 90, 353–361.
- Fee, M.S., Mitra, P.P., and Kleinfeld, D. (1997). Central versus peripheral determinants of patterned spike activity in rat vibrissa cortex during whisking. *J. Neurophysiol.* 78, 1144–1149.
- Felleman, D.J., and Van Essen, D.C. (1991). Distributed hierarchical processing in the primate cerebral cortex. *Cereb. Cortex* 1, 1–47.
- Ferezou, I., Haiss, F., Gentet, L.J., Aronoff, R., Weber, B., and Petersen, C.C. (2007). Spatiotemporal dynamics of cortical sensorimotor integration in behaving mice. *Neuron* 56, 907–923.
- Fetz, E.E., and Baker, M.A. (1973). Operantly conditioned patterns on precentral unit activity and correlated responses in adjacent cells and contralateral muscles. *J. Neurophysiol.* 36, 179–204.
- Gibson, J.J. (1962). Observations on active touch. *Psychol. Rev.* 69, 477–491.
- Grinevich, V., Brecht, M., and Osten, P. (2005). Monosynaptic pathway from rat vibrissa motor cortex to facial motor neurons revealed by lentivirus-based axonal tracing. *J. Neurosci.* 25, 8250–8258.
- Groh, A., Meyer, H.S., Schmidt, E.F., Heintz, N., Sakmann, B., and Krieger, P. (2010). Cell-type specific properties of pyramidal neurons in neocortex underlying a layout that is modifiable depending on the cortical area. *Cereb. Cortex* 20, 826–836.
- Hattox, A.M., and Nelson, S.B. (2007). Layer V neurons in mouse cortex projecting to different targets have distinct physiological properties. *J. Neurophysiol.* 98, 3330–3340.
- Hattox, A.M., Priest, C.A., and Keller, A. (2002). Functional circuitry involved in the regulation of whisker movements. *J. Comp. Neurol.* 442, 266–276.
- Helmchen, F., Svoboda, K., Denk, W., and Tank, D.W. (1999). In vivo dendritic calcium dynamics in deep-layer cortical pyramidal neurons. *Nat. Neurosci.* 2, 989–996.
- Hoffer, Z.S., Hoover, J.E., and Alloway, K.D. (2003). Sensorimotor corticocortical projections from rat barrel cortex have an anisotropic organization that facilitates integration of inputs from whiskers in the same row. *J. Comp. Neurol.* 466, 525–544.
- Hoffer, Z.S., Arantes, H.B., Roth, R.L., and Alloway, K.D. (2005). Functional circuits mediating sensorimotor integration: quantitative comparisons of projections from rodent barrel cortex to primary motor cortex, neostriatum, superior colliculus, and the pons. *J. Comp. Neurol.* 488, 82–100.
- Hoogland, P.V., Welker, E., and Van der Loos, H. (1987). Organization of the projections from barrel cortex to thalamus in mice studied with Phaseolus vulgaris-leucoagglutinin and HRP. *Exp. Brain Res.* 68, 73–87.
- Hooks, B.M., Hires, S.A., Zhang, Y.X., Huber, D., Petreanu, L., Svoboda, K., and Shepherd, G.M. (2011). Laminar analysis of excitatory local circuits in vibrissal motor and sensory cortical areas. *PLoS Biol.* 9, e1000572. 10.1371/journal.pbio.1000572.
- Hutson, K.A., and Masterton, R.B. (1986). The sensory contribution of a single vibrissa's cortical barrel. *J. Neurophysiol.* 56, 1196–1223.
- Izraeli, R., and Porter, L.L. (1995). Vibrissal motor cortex in the rat: connections with the barrel field. *Exp. Brain Res.* 104, 41–54.
- Johnston, D., Magee, J.C., Colbert, C.M., and Christie, B.R. (1996). Active properties of neuronal dendrites. *Annu. Rev. Neurosci.* 19, 165–186.
- Kleinfeld, D., Berg, R.W., and O'Connor, S.M. (1999). Anatomical loops and their electrical dynamics in relation to whisking by rat. *Somatosens. Mot. Res.* 16, 69–88.
- Kleinfeld, D., Sachdev, R.N., Merchant, L.M., Jarvis, M.R., and Ebner, F.F. (2002). Adaptive filtering of vibrissa input in motor cortex of rat. *Neuron* 34, 1021–1034.
- Knutsen, P.M., Pietr, M., and Ahissar, E. (2006). Haptic object localization in the vibrissal system: behavior and performance. *J. Neurosci.* 26, 8451–8464.
- Komiyama, T., Sato, T.R., O'Connor, D.H., Zhang, Y.X., Huber, D., Hooks, B.M., Gabbito, M., and Svoboda, K. (2010). Learning-related fine-scale specificity imaged in motor cortex circuits of behaving mice. *Nature* 464, 1182–1186.
- Krupa, D.J., Matell, M.S., Brisben, A.J., Oliveira, L.M., and Nicolelis, M.A. (2001). Behavioral properties of the trigeminal somatosensory system in rats performing whisker-dependent tactile discriminations. *J. Neurosci.* 21, 5752–5763.
- Lalazar, H., and Vaadia, E. (2008). Neural basis of sensorimotor learning: modifying internal models. *Curr. Opin. Neurobiol.* 18, 573–581.
- Larkum, M.E., Senn, W., and Lüscher, H.R. (2004). Top-down dendritic input increases the gain of layer 5 pyramidal neurons. *Cereb. Cortex* 14, 1059–1070.
- Larkum, M.E., Nevian, T., Sandler, M., Polsky, A., and Schiller, J. (2009). Synaptic integration in tuft dendrites of layer 5 pyramidal neurons: a new unifying principle. *Science* 325, 756–760.
- Lefort, S., Tamm, C., Floyd Sarria, J.C., and Petersen, C.C. (2009). The excitatory neuronal network of the C2 barrel column in mouse primary somatosensory cortex. *Neuron* 61, 301–316.
- Li, C.X., and Waters, R.S. (1991). Organization of the mouse motor cortex studied by retrograde tracing and intracortical microstimulation (ICMS) mapping. *Can. J. Neurol. Sci.* 18, 28–38.
- London, M., and Häusser, M. (2005). Dendritic computation. *Annu. Rev. Neurosci.* 28, 503–532.
- Lu, S.M., and Lin, R.C.S. (1993). Thalamic afferents of the rat barrel cortex: a light- and electron-microscopic study using *Phaseolus vulgaris* leucoagglutinin as an anterograde tracer. *Somatosens. Mot. Res.* 10, 1–16.
- Lübke, J., and Feldmeyer, D. (2007). Excitatory signal flow and connectivity in a cortical column: focus on barrel cortex. *Brain Struct. Funct.* 212, 3–17.
- Luo, L., Callaway, E.M., and Svoboda, K. (2008). Genetic dissection of neural circuits. *Neuron* 57, 634–660.
- Magee, J.C., and Johnston, D. (1995). Characterization of single voltage-gated Na⁺ and Ca²⁺ channels in apical dendrites of rat CA1 pyramidal neurons. *J. Physiol.* 487, 67–90.
- Manns, I.D., Sakmann, B., and Brecht, M. (2004). Sub- and suprathreshold receptive field properties of pyramidal neurones in layers 5A and 5B of rat somatosensory barrel cortex. *J. Physiol.* 556, 601–622.

- Matyas, F., Sreenivasan, V., Marbach, F., Wacongne, C., Barsy, B., Mateo, C., Aronoff, R., and Petersen, C.C. (2010). Motor control by sensory cortex. *Science* 330, 1240–1243.
- Mehta, S.B., Whitmer, D., Figueroa, R., Williams, B.A., and Kleinfeld, D. (2007). Active spatial perception in the vibrissa scanning sensorimotor system. *PLoS Biol.* 5, e15. 10.1371/journal.pbio.0050015.
- Meyer, H.S., Wimmer, V.C., Hemberger, M., Bruno, R.M., de Kock, C.P., Frick, A., Sakmann, B., and Helmstaedter, M. (2010a). Cell type-specific thalamic innervation in a column of rat vibrissal cortex. *Cereb. Cortex* 20, 2287–2303.
- Meyer, H.S., Wimmer, V.C., Oberlaender, M., de Kock, C.P., Sakmann, B., and Helmstaedter, M. (2010b). Number and laminar distribution of neurons in a thalamocortical projection column of rat vibrissal cortex. *Cereb. Cortex* 20, 2277–2286.
- Mitchinson, B., Martin, C.J., Grant, R.A., and Prescott, T.J. (2007). Feedback control in active sensing: rat exploratory whisking is modulated by environmental contact. *Proc. Biol. Sci.* 274, 1035–1041.
- Miyashita, E., Keller, A., and Asanuma, H. (1994). Input-output organization of the rat vibrissal motor cortex. *Exp. Brain Res.* 99, 223–232.
- Nagel, G., Szellas, T., Huhn, W., Kateriya, S., Adeishvili, N., Berthold, P., Ollig, D., Hegemann, P., and Bamberg, E. (2003). Channelrhodopsin-2, a directly light-gated cation-selective membrane channel. *Proc. Natl. Acad. Sci. USA* 100, 13940–13945.
- Nguyen, Q.T., and Kleinfeld, D. (2005). Positive feedback in a brainstem tactile sensorimotor loop. *Neuron* 45, 447–457.
- Nudo, R.J., and Masterton, R.B. (1990). Descending pathways to the spinal cord, III: Sites of origin of the corticospinal tract. *J. Comp. Neurol.* 296, 559–583.
- O'Connor, S.M., Berg, R.W., and Kleinfeld, D. (2002). Coherent electrical activity between vibrissa sensory areas of cerebellum and neocortex is enhanced during free whisking. *J. Neurophysiol.* 87, 2137–2148.
- O'Connor, D.H., Huber, D., and Svoboda, K. (2009). Reverse engineering the mouse brain. *Nature* 461, 923–929.
- O'Connor, D.H., Clack, N.G., Huber, D., Komiyama, T., Myers, E.W., and Svoboda, K. (2010a). Vibrissa-based object localization in head-fixed mice. *J. Neurosci.* 30, 1947–1967.
- O'Connor, D.H., Peron, S.P., Huber, D., and Svoboda, K. (2010b). Neural activity in barrel cortex underlying vibrissa-based object localization in mice. *Neuron* 67, 1048–1061.
- Paxinos, G.F., and Franklin, K.B.J. (2004). *The Mouse Brain in Stereotaxic Coordinates, Compact Second Edition* (Amsterdam: Elsevier).
- Petersen, C.C. (2007). The functional organization of the barrel cortex. *Neuron* 56, 339–355.
- Petreanu, L., Huber, D., Sobczyk, A., and Svoboda, K. (2007). Channelrhodopsin-2-assisted circuit mapping of long-range callosal projections. *Nat. Neurosci.* 10, 663–668.
- Petreanu, L., Mao, T., Sternson, S.M., and Svoboda, K. (2009). The subcellular organization of neocortical excitatory connections. *Nature* 457, 1142–1145.
- Porter, L.L., and White, E.L. (1983). Afferent and efferent pathways of the vibrissal region of primary motor cortex in the mouse. *J. Comp. Neurol.* 214, 279–289.
- Rocco, M.M., and Brumberg, J.C. (2007). The sensorimotor slice. *J. Neurosci. Methods* 162, 139–147.
- Sato, T.R., and Svoboda, K. (2010). The functional properties of barrel cortex neurons projecting to the primary motor cortex. *J. Neurosci.* 30, 4256–4260.
- Schubert, D., Kötter, R., Zilles, K., Luhmann, H.J., and Staiger, J.F. (2003). Cell type-specific circuits of cortical layer IV spiny neurons. *J. Neurosci.* 23, 2961–2970.
- Schubert, D., Kötter, R., Luhmann, H.J., and Staiger, J.F. (2006). Morphology, electrophysiology and functional input connectivity of pyramidal neurons characterizes a genuine layer Va in the primary somatosensory cortex. *Cereb. Cortex* 16, 223–236.
- Shaner, N.C., Campbell, R.E., Steinbach, P.A., Giepmans, B.N., Palmer, A.E., and Tsien, R.Y. (2004). Improved monomeric red, orange and yellow fluorescent proteins derived from *Discosoma* sp. red fluorescent protein. *Nat. Biotechnol.* 22, 1567–1572.
- Shepherd, G.M., and Harris, K.M. (1998). Three-dimensional structure and composition of CA3→CA1 axons in rat hippocampal slices: implications for presynaptic connectivity and compartmentalization. *J. Neurosci.* 18, 8300–8310.
- Shepherd, G.M.G., and Svoboda, K. (2005). Laminar and columnar organization of ascending excitatory projections to layer 2/3 pyramidal neurons in rat barrel cortex. *J. Neurosci.* 25, 5670–5679.
- Shepherd, G.M., Pologruto, T.A., and Svoboda, K. (2003). Circuit analysis of experience-dependent plasticity in the developing rat barrel cortex. *Neuron* 38, 277–289.
- Shepherd, G.M.G., Stepanyants, A., Bureau, I., Chklovskii, D.B., and Svoboda, K. (2005). Geometric and functional organization of cortical circuits. *Nat. Neurosci.* 8, 782–790.
- Sporns, O., and Kötter, R. (2004). Motifs in brain networks. *PLoS Biol.* 2, e369. 10.1371/journal.pbio.0020369.
- Stettler, D.D., Yamahachi, H., Li, W., Denk, W., and Gilbert, C.D. (2006). Axons and synaptic boutons are highly dynamic in adult visual cortex. *Neuron* 49, 877–887.
- Svoboda, K., Hooks, B.M., and Shepherd, G.M. (2010). Barrel cortex. In *Handbook of Brain Microcircuits*, G.M. Shepherd and S. Grillner, eds. (Oxford: Oxford University Press).
- Tennant, K.A., Adkins, D.L., Donlan, N.A., Asay, A.L., Thomas, N., Kleim, J.A., and Jones, T.A. (2011). The organization of the forelimb representation of the C57BL/6 mouse motor cortex as defined by intracortical microstimulation and cytoarchitecture. *Cereb. Cortex* 21, 865–876.
- Veinante, P., and Deschênes, M. (2003). Single-cell study of motor cortex projections to the barrel field in rats. *J. Comp. Neurol.* 464, 98–103.
- Vogt, B.A., and Pandya, D.N. (1978). Cortico-cortical connections of somatic sensory cortex (areas 3, 1 and 2) in the rhesus monkey. *J. Comp. Neurol.* 177, 179–191.
- Weiler, N., Wood, L., Yu, J., Solla, S.A., and Shepherd, G.M. (2008). Top-down laminar organization of the excitatory network in motor cortex. *Nat. Neurosci.* 11, 360–366.
- Welker, E., Hoogland, P.V., and Van der Loos, H. (1988). Organization of feedback and feedforward projections of the barrel cortex: a PHA-L study in the mouse. *Exp. Brain Res.* 73, 411–435.
- White, E.L. (2002). Specificity of cortical synaptic connectivity: emphasis on perspectives gained from quantitative electron microscopy. *J. Neurocytol.* 31, 195–202.
- White, E.L., and DeAmicis, R.A. (1977). Afferent and efferent projections of the region in mouse SmL cortex which contains the posteromedial barrel subfield. *J. Comp. Neurol.* 175, 455–482.
- Wolpert, D.M., Ghahramani, Z., and Jordan, M.I. (1995). An internal model for sensorimotor integration. *Science* 269, 1880–1882.
- Zhang, Y.P., and Oertner, T.G. (2007). Optical induction of synaptic plasticity using a light-sensitive channel. *Nat. Methods* 4, 139–141.